Investigation of a trifold interaction mechanism of shock, vortex, and dust using a DG method in a two-fluid model framework

Omid Ejtehadi [a,b], Amin Rahimi [a], R. S. Myong[a]*

[a] *School of Mechanical and Aerospace Engineering, and ACTRC, Gyeongsang National University, Jinju, Gyeongnam 52828, South Korea*

[b] *Supercomputing Modeling and Simulation Center, Korea Institute of Science and Technology Information (KISTI), Daejeon 305-806, South Korea*

*Corresponding author: Tel +82 55 772-1645 (Fax 1580); *myong@gnu.ac.kr*

Abstract

We investigate a trifold interaction mechanism of shock, vortex, and dust by solving the dusty Schardin's problem. A modal discontinuous Galerkin method was developed for solving the two-fluid model of the dusty gases. We focused on larger-scale wave patterns and smaller-scale vortexlets under the addition of dust particles. The dynamics of the shock-vortex interaction in a dusty medium was found substantially different from a pure gas equivalent. The main differences are the acceleration or deceleration of the shock waves, and attenuation or diminishing of the slip lines. It was also demonstrated how the solid phase with various particulate loadings and particle diameters affects the dynamics of the vortexlets. Two different trends related to the transient formation and attenuation of the main vortex and vortexlets were identified. It was shown that the enstrophy behavior is directly affected by the diameter and particulate loading of particles that are seeded in the domain.

Keywords: dusty gas, two-fluid model, shock-vortex interaction, dust-vortexlet interaction, discontinuous Galerkin

1 Introduction

The interaction of shocks and vortices–two fundamental fluid dynamics phenomena–has been a topic of interest for decades. Understanding such interactions is essential in various technological and environmental applications, including noise generated by supersonic jets, shock-enhanced mixing (especially in non-premixed supersonic combustion), strake-wing configurations, and compressors operating near their stability limits [1-5].

The importance and intrinsic complexity of the problem have motivated various experimental and numerical investigations in different contexts. Extensive investigations have focused on the acoustic wave generated from this interaction, both in early experiments [6, 7] and numerical simulations [8]. Weeks and Dosanjh [9] applied Stratton's method of integrating the governing nonhomogeneous wave equation in two dimensions to the shock-vortex problem, to expand upon the concept of noise generation by shock-vortex interaction. Almost thirty years later, Inoue and Hattori [10], in a paper with the same title, studied the mechanics of the interaction between a single vortex and a pair of vortices and a shock wave at an early stage of interaction by solving Navier-Stokes equations via a finite difference method. They reported that sound generation is related to the generation of reflected shock waves. So far, several numerical studies have investigated the problem using different models developed in the finite element [11], finite difference [4, 12, 13], finite volume [14-19], and discontinuous Galerkin [20, 21] frameworks.

Among the aforementioned studies, some analyzed the interaction of a planar shock with a single vortex [12], a pair of vortices [4], and a vortex ring [14]. The interaction of a planar shock with a strong vortex was also investigated [13, 17].

Another group of researchers considered the shock-vortex problem in Schardin’s problem, named after the experiments done by Schardin [22], i.e., the interaction of a reflected shock with the vortex formed after the passage of an incident shock from a wedge, with the help of various numerical tools, e.g., finite element method-flux corrected transport (FEM-FCT) [11], high-resolution TVD method and adaptive quadrilateral grid refinement in a finite volume framework [15, 16], fifth-order MUSCL interpolation with the ASUM+ flux function [18]. Among these works, which mostly solved inviscid Euler equations, Halder *et al*. [18] applied the Navier-Stokes equation and focused on vortices generated by the Kelvin–Helmholtz instability.

More recently, the problem has been investigated in microscale [23]; the viscous attenuation of the vortex distinguishes the microscale problem from the macroscale counterpart. Koffi *et al*. [23] considered the interaction of a planar shock and a vortex using the direct simulation Monte Carlo (DSMC) method. Xiao and Myong [20] approached the problem by solving conservation laws in conjunction with an implicit type second-order constitutive relation using a mixed discontinuous Galerkin (DG) formulation. Singh *et al*. [21] investigated the problem, including the role of the rotational mode of the diatomic and polyatomic gas molecules, by solving the conservation laws in conjunction with constitutive equations derived from the Boltzmann-Curtiss kinetic equations. It was found that in microscale, the quadrupolar acoustic wave structure disappears, the dissipation rate increases, and the enstrophy decreases or increases depending on the degree of interaction. A survey of some of the important studies on the shock-vortex interaction is provide in **Table 1**.

On the other hand, when these two flow structures (shock and vortex) form in a dusty environment, the dust-gas interaction can significantly affect the dynamics of the flow. The interaction of shocks with dusty or granular environments has been a topic of interest for decades [24-31]. A great deal of research has been conducted on the interaction of dust particles with vortices, especially in the context of free mixing layers. The dispersion of particles in free shear layers can be observed in a variety of applications including coating by aerosols, chemical reactors and combustors, boilers and heat exchangers, fluidized beds, and sedimentation, where it has been shown to be due to coherent, large scale vortical structures [32-38]. The research extends from engineering-oriented applications [35, 38, 39] to more fundamental studies, such as the investigation of the underlying physics of the interaction of vortices and particles in flows past bluff bodies [32, 34, 40-42] and turbulent particle-laden flows [43]. For more information on this topic, interested readers may refer to [44] and the references therein.

Dust entrainment by a planar shock-induced vortex, which has been studied in a number of experimental and numerical works, is another relevant subject. Examples include finite difference investigation of the problem by Ben-Dor [26], a TVD scheme for the gas, and the Eulerian differencing method for particles by Fedorov and Kharlamova [45], and a second-order flux corrected transport algorithm for the gas along with a Lagrangian approach for the solid particles by Ilea *et al*. [46]. In this problem, the passage of a planar shock over a loosely packed dust layer forms a curved cloud of entrained particles that are interacting with the deformed shock. However, there is no further interaction between the shock with the vortex, and it is only the dust particles that are engaged in the shock-induced vortex.

As illustrated above, the interactions of vortices and shocks with dusty environments have been investigated from different points of view. However, very few attempts have been made on analysis of the shock-vortex interaction in a dusty environment. *Therefore, we focus on investigation of the trifold interactions of dust particles with shocks and vortices.* For this purpose, the so-called Schardin's problem in the presence of dust particles (which hereafter is referred to as the dusty Schardin's problem) is considered, and the effect of the particulate phase on the shock-vortex interaction is investigated. For this undertaking, a high-order discontinuous Galerkin solver in the Eulerian-Eulerian framework is developed. The developed solver has been validated for various benchmark problems by Ejtehadi *et al*. [47].

It is well-known that particles inside a vortex will follow a pattern from the vortex core and concentrate on the edges of the vortex. Moreover, in dusty gas flows, the presence of relaxation regions and the complex mechanisms of wave patterns including pseudo-compound waves (a reflected shock attached to the rarefaction wave) and composite waves (a contact discontinuity attached to the relaxation zone) can be observed, which affect the dynamics of the flow. In Schardin's problem, a traveling shock wave passes by a compression corner forming different types of Mach reflections depending on the shock Mach number and wall inclination angle. When the shock front passes the wedge, two counter-rotating vortices will be created behind the triangular prism, which interact with the reflection of the shock wave from the symmetry plane.

Among the three major models used to model the particulate flows, i.e., the Eulerian-Eulerian, Eulerian-Lagrangian, and mixture models, the Eulerian-Eulerian (also simply called the Eulerian) model was selected because of the efficiency the model offers in terms of computational cost. In addition, the model can cover a broader range of particulate flow regimes. However, Eulerian models (in their original form) are not suitable for solving systems with particle size distributions. **Table 2** provides a comparison of the two general categories of models for simulating multiphase flows, summarizing the merits and drawbacks of each model**.** Apart from the advantages and disadvantages each method offers, it is still necessary to take the target regime of interest into account during the process of selecting the mathematical model. **Fig. 1** illustrates the selection of a suitable mathematical model based on the loading level.

Recent advances in computational methods and computer resources have led to the successful application of the DG method to various classes of problems such as compressible and incompressible flows, aeroacoustics, magneto-hydrodynamics, and many more [48]. The method has recently found its way into multiphase flow problems. Examples include the development of a robust high order DG method for compressible multiphase flows based on the Baer and Nunziato type systems by Franquet and Perrier [49], application of the DG method to conservative level set equations for interphase capturing in multiphase flows [50], development of a Runge-Kutta DG method together with the front tracking method for solving two-medium gas-gas and gas-liquid flows [51], development of a vertex-based DG method of multiphase compositional flow [52] and development of a modal DG method for dilute dusty gas flows [47] and dusty/granular gas flows in thermal non-equilibrium [53].

The Euler equations for the gas phase, and pressureless Euler equations for the solid phase, are solved using a modal discontinuous Galerkin approach. The aim is to provide insight into how the presence of dust particles can affect the complex shock-vortex interaction in Schardin's problem. In addition to investigating the interactions of discontinuities and the vortex with dust particles (which can be explained in larger length-scales), the effects of solid particles on the smaller-scale phenomena in the vicinity of the wedge are also examined. It is worth mentioning that the proposed method can be applied in various industrial applications ranging from compressible flow through porous media [54-56] to petroleum engineering [57].

2 Mathematical modeling and numerical procedure

2.1 Two-fluid model (TFM)

In the majority of Eulerian models that consider dusty gas flows, the gas phase is considered to be compressible, following the perfect-gas law, while the solid phase is considered incompressible [28, 29, 58, 59]. Inter-particle collisions are neglected (thus no pressure term in the conservation law of solid phase) and the particles are assumed to be uniform sized spheres with a constant diameter and microscopic density. The specific heat of the particle's material is constant, and the temperature is uniform within each particle. Moreover, particles are considered to be inert, and their thermal and Brownian motion is neglected. Furthermore, the gravitational and buoyant forces, the turbulence effects and the effect of particles' wakes are considered to be negligible. In this model, the number density of the particles should be large enough not to violate the continuum assumption.

It is worth mentioning that the inter-particle or wall-particle collisions can be taken into account in another subcategory of the Eulerian models, usually referred to in the literature as the Eulerian-granular model. In this category, models based on the so-called *kinetic theory of granular flows* (KTGF) have been shown to provide accurate predictions of the solid phase [60-66].

2.2 Governing equations of the gas and solid phases in TFM

Under the above-mentioned conditions, the conservation laws can be written as follows:

For the gas phase,

$$\partial_t \mathbf{U}_g + \nabla \cdot \mathbf{F}_g = \mathbf{S} \tag{1}$$

$$\mathbf{U}_g = \begin{bmatrix} \alpha_g \rho_g \\ \alpha_g \rho_g \mathbf{u}_g \\ \alpha_g \rho_g E_g \end{bmatrix}, \quad \mathbf{F}_g = \begin{bmatrix} \alpha_g \rho_g \mathbf{u}_g \\ \alpha_g \rho_g \mathbf{u}_g \mathbf{u}_g + p\mathbf{I} \\ (\alpha_g \rho_g E_g + p)\mathbf{u}_g \end{bmatrix}, \quad \mathbf{S} = \begin{bmatrix} 0 \\ D_{g,s}(\mathbf{u}_s - \mathbf{u}_g) \\ D_{g,s}(\mathbf{u}_s - \mathbf{u}_g)\mathbf{u}_s + Q_g(T_s - T_g) \end{bmatrix} \tag{2}$$

$$E_g = c_v T_g + \frac{1}{2}\left|\mathbf{u}_g\right|^2 \tag{3}$$

and for the solid phase,

$$\partial_t \mathbf{U}_s + \nabla \cdot \mathbf{F}_s = -\mathbf{S} \tag{4}$$

$$\mathbf{U}_s = \begin{bmatrix} \alpha_s \rho_s \\ \alpha_s \rho_s \mathbf{u}_s \\ \alpha_s \rho_s E_s \end{bmatrix}, \quad \mathbf{F}_s = \begin{bmatrix} \alpha_s \rho_s \mathbf{u}_s \\ \alpha_s \rho_s \mathbf{u}_s \mathbf{u}_s \\ (\alpha_s \rho_s E_s)\mathbf{u}_s \end{bmatrix} \tag{5}$$

$$E_s = c_m T_p + \frac{1}{2}\left|\mathbf{u}_s\right|^2 \tag{6}$$

$$\alpha_g + \alpha_s = 1. \tag{7}$$

Here the **U**, **F**, and **S** are the vectors of conservative variables, fluxes, and source terms, respectively. The variables t, α, ρ, $\mathbf{u}$, E, p, T, D, and Q represent time, volume fraction, density, velocity vector, total energy, pressure, temperature, interphase drag and heat flux, respectively. The dust density ρ_s is assumed to be constant. c_v and c_m are the specific heat capacity of the gas at constant volume and the specific heat of the particle material. The equation of state expresses the gas pressure in terms of other gas properties:

$$p = \rho_g R T_g \tag{8}$$

where R is the gas constant.

According to Miura and Glass [67], the drag force that solid particles exert on the gas phase can be expressed as

$$D_{g,s} = \frac{3}{4} C_D \frac{\alpha_s \rho_g}{d} \left| \mathbf{u}_g - \mathbf{u}_s \right| \tag{9}$$

in which d is the particle diameter and C_D is the drag coefficient computed as a function of the Reynolds number based on the particle diameter and relative velocity of the particle to the gas (i.e. $\mathrm{Re}_d = \rho_g d \left| \mathbf{u}_g - \mathbf{u}_s \right| / \mu_g$). The drag coefficient can then be given by a well-established semi-empirical correlation [68],

$$C_D = \begin{cases} \dfrac{24}{\mathrm{Re}_d}\left(1 + 0.15\,\mathrm{Re}^{0.687}\right), & \text{if} \quad \mathrm{Re}<1000 \\ 0.44, & \text{if} \quad \mathrm{Re}>1000. \end{cases} \tag{10}$$

To derive more accurate regime-dependent drag coefficients for the spherical particles, interested readers can refer to the recent comprehensive review from Tiwari *et al*. [69] on flow past a single stationary sphere.

Heat transfer, which is proportional to temperature difference, can be expressed as a function of the Nusselt number [28],

$$Q_g = \frac{6\mathrm{Nu}\kappa_g}{d^2} \alpha_s (T_g - T_s) \tag{11}$$

$$\mathrm{Nu} = 2 + 0.65\,\mathrm{Re}_d^{\frac{1}{2}}\,\mathrm{Pr}^{\frac{1}{3}}\ ,\ \mathrm{Pr} = \frac{c_p \mu_g}{\kappa_g}. \tag{12}$$

Here μ_g and κ_g represent the viscosity and thermal conductivity of the gas, respectively.

2.3 A modal discontinuous Galerkin method for dusty gas flows

The equations of the dusty gas flows described in the previous section are discretized using a modal discontinuous Galerkin (DG) method. The essential parts of the modal unstructured DG method developed in the present work—in particular, high order accuracy and positivity/monotonicity preserving property—are summarized in [47].

The mathematical model of interest in the present work can be written in a compact form;

$$\partial_t \mathbf{U} + \nabla \cdot \mathbf{F}(\mathbf{U}) = \mathbf{S}(\mathbf{U}) \qquad \text{in} \left[(t, \Omega) \middle| t \in (0, \infty), \Omega \subset \mathbb{R} \right] \tag{13}$$

where Ω denotes a bounded domain, and **U**, **F**, **S** are conservative variables for vector, flux tensor, and source terms vector, respectively. The solution domain can be decomposed by a group of non-overlapping elements, $\Omega = \Omega_1 \cup \Omega_2 \cup \ldots \Omega_n$, in which n is the number of elements. By multiplying a weighting function φ_i into the conservative laws (16) and integrating over the control volume for each element, the following formulation can be derived:

$$\int_{\Omega_k} \left[\partial_t \mathbf{U} \varphi(\mathbf{x}) + \nabla \cdot F(\mathbf{U}) \varphi(\mathbf{x}) - S(\mathbf{U}) \varphi(\mathbf{x}) \right] d\Omega = 0. \tag{14}$$

To construct a discretized system of the conservation laws, the global spatial domain Ω can be approximated by Ω_h where $\Omega_h \rightarrow \Omega$ as $h \rightarrow 0$. The approximated domain, which is a tessellation of the space by bounded elementary control volumes, $\mathcal{T}_h = \{\Omega_e\}$, is filled with n number of non-overlapping elements $\Omega_e \in \mathcal{T}_h$. The exact solution of the governing equations can be approximated by the numerical solution in every local element as

$$\mathbf{U}(\mathbf{x}, t) \approx \mathbf{U}_h = \sum_{e=1}^{n} \mathbf{U}_h^e(\mathbf{x}, t) \equiv \mathbf{U}_h^1 + \ldots + \mathbf{U}_h^n. \tag{15}$$

By splitting the integral over Ω_h into a series of integrals over the sub-elements and applying the integration by part as well as divergence theorem to the equation (14), the elemental formulation reads as

$$\begin{aligned} &\int_{\Omega_k} \partial_t \mathbf{U}_h \varphi_i(\mathbf{x}) \mathrm{d}\Omega_k + \oint_{\partial\Omega_k} \varphi_i(\mathbf{x}) \partial_{\mathbf{x}} \mathbf{F}(\mathbf{U}_h) \cdot \hat{n} d\sigma - \int_{\Omega_k} \nabla \varphi_i(\mathbf{x}) \cdot \mathbf{F}(\mathbf{U}_h) \mathrm{d}\Omega_k \\ &= \int_{\Omega_k} \varphi_i(\mathbf{x}) \mathbf{S}(\mathbf{U}_h) \mathrm{d}\Omega_k \end{aligned} \tag{16}$$

where $\hat{n}$ is the outward normal vector of the element interface, and $\mathbf{U}_h$ is the p-exact polynomial approximated solutions of the U on the discretized domain of Ω_h. $\mathbf{U}_h$ can be expressed as the polynomial field that sums the multiplication of the local degree of freedom with the corresponding smooth polynomials of degree P in the standard element:

$$\mathbf{U}_h = \sum_{i}^{P} a_i(t) \varphi_i(\mathbf{x}). \tag{17}$$

Here $a_i(t)$ and $\varphi(\mathrm{x})$ denote the local degree of freedom and the basis function, which can be chosen to be any continuous polynomial function, respectively.

2.3.1 Positivity and monotonicity preserving schemes

High order conservative schemes, including the DG scheme introduced in the previous section, usually suffer from non-physical negative density or pressure. This situation leads to the ill-posedness of the system and numerical breakdowns as a consequence. When source terms are added to account for chemical reactions, gravity, or the interaction of phases in the conservation laws, as in the present case, the potential of encountering negative density or pressure during numerical simulation increases. Therefore, it becomes necessary to apply efficient positivity preserving schemes to prevent the numerical breakdown.

In the present work, the positivity preserving scheme of Zhang and Shu [70] for compressible Euler equations was applied to ensure the positivity of the density and pressure fields, while maintaining higher-order accuracy. Our numerical investigations show that a simple application of the positivity preserving scheme is not enough to develop a stable scheme, especially in the presence of strong shock waves. The situation deteriorates when the multiphase system with source terms is being solved. In the present study, both the limiter from Zhang and Shu [71] for one-dimensional cases, and the limiter of Barth and Jespersen [72], which was initially devised for a finite volume framework, are applied. It is important to note that any TVD/MUSCL type scheme can degrade the order of accuracy in the smooth regions of the solution, unless a pragmatic shock detection scheme is introduced.

2.3.2 Numerical fluxes for the multiphase solver

The choice of numerical flux can determine the stability and accuracy of the numerical method. In order to obtain a stable scheme, the numerical flux should be consistent as well as conservative. Here, the local Lax-Friedrichs (LLF) (or Rusanov [73]) and rotated-Harten-Lax-van Leer [74] fluxes, both of which are known to be simple and free from carbuncle phenomenon, were implemented. Implementing the inviscid numerical flux is analogous to the well-established FVM procedure, and the details of the implementation can be omitted.

It should be noted that the AUSM family [75, 76] schemes have been widely used in many previous numerical works to simulate the dust phase. However, we aim to use the same flux scheme for both phases to be consistent. This may raise numerical difficulties when the solid pressure term in the model equations is not included. In such a case, even though the system has real eigenvalues, they are not distinct; thus, the system becomes degenerate. Few approaches have been proposed to deal with this numerical issue in the past. Nevertheless, in the subsection *2.3.4*, a simple, easy to implement, and yet effective method to circumvent this issue will be proposed.

2.3.3 Boundary condition

When implementing boundary conditions in two-fluid or multi-fluid systems, a different set of conditions is required for each phase. For the investigated problem, an adiabatic, impermeable, inviscid wall boundary condition is applied for both phases [59]. Other choices in boundary conditions, such as the adherence condition or reflection conditions, are also viable for the solid phase [77]. When the viscous system of conservation laws (e.g., Navier-Stokes-Fourier) is considered, it is necessary to use a non-slip boundary condition for the gas phase and a slip boundary condition for the solid phase.

2.3.4 Complexities associated with the numerical solution of TFM of the dusty gases

The investigated system of equations differs from conventional conservation laws in two respects: 1) The presence of the source terms, and 2) the non-existence of a pressure term in the equations of the solid phase. These distinctions impose some complexities on the numerical simulations. Here remedies to these issues are briefly addressed.

It was well-known that the stiff relaxation terms in balance laws (i.e., strictly hyperbolic systems with source terms) lead to disparate relaxation times, which in turn result in severe numerical difficulties. In the two-fluid model, in addition to the time scale related to convection, a much smaller relaxation time scale exists that inevitably imposes smaller time steps on the numerical solver. The use of a slower time scale in such problems can cause severe numerical instability. Methods such as operator splitting and the zero-relaxation limit have been used to remedy the issue. However, the choice of orthogonal basis functions in our method greatly simplifies the contribution of the high order moments of the polynomial approximate solution to the source-term related vector. More detailed discussions on this issue can be found in [47].

Furthermore, the non-strictly hyperbolic nature of the equation of the dust phase (due to the non-existence of a pressure term) can impose severe difficulties for the numerical solver (mainly when finite volume schemes are applied). The issue can be circumvented either by considering the dispersed phase to be incompressible and adding a pressure term for statistical purposes [78, 79], or by considering both phases compressible. The former approach can yield a hyperbolic system but is not physically justifiable. On the other hand, the latter method can lead to unrealistic results in many two-phase flow problems [80].

In this study, we apply an efficient and easy-to-implement method, which has been previously developed by the authors. The idea is to add and subtract a pressure-related term to the momentum and energy equations of the dust phase. Even though this manipulation does not have any mathematical consequences, from a numerical point of view, the new system has an obvious advantage, recovering the strict hyperbolicity of the equation. More details can be found in [53].

3 Results and discussion

Different scenarios for defining the dusty Schardin's problem can be considered. The dust can be initialized uniformly on both sides of the diaphragm, or it can be present only on the right-hand side of the membrane. It is also possible that the domain is initialized with dust just after the compression corner where the vortex starts to form. The initialization may affect the evolution of flow structures. In this work, we chose the case where the whole domain is initialized with a uniform distribution of dust grains.

In **Fig. 2** (a) and (b), the initial and boundary conditions for the Schardin's problem in single-phase and multiphase cases are summarized, respectively. The selected geometry is an equilateral triangle with a base of 20 cm. Different scenarios for defining the dusty Schardin's problem can be considered. The dust can be initialized uniformly on both sides of the diaphragm, or it can be present only on the right-hand side of the membrane. It is also possible that the domain is initialized with dust just after the compression corner where the vortex starts to form. The initialization may affect the evolution of flow structures. In this work, we chose the case where the whole domain is initialized with a uniform distribution of dust grains.

Fig. 2 (c) provides a schematic of the various types of discontinuities and other compressible fluid features that are present in Schardin's problem. As a result of the impingement and therefore the reflection and deflection of the moving planar shock over the wedge, various features such as Mach stems, slip lines, Mach triple points, vortices, and vortexlets emerge in the flowfield, which makes the study of the problem more interesting. In the following subsections, after validating the developed numerical tool for this specific problem, we investigate the effects of the addition of dust particles on the behavior of the featuring structures. The values of the parameters used in the simulations are tabulated in **Table 3**.

3.1 Verification and validation of results

The developed computational tool has been extensively verified and validated in various problems for both pure gas and dusty gas models, in [47, 53, 81]. The pure gas solutions in the Sod shock tube problem, single-Mach reflection in compression corner, underexpanded jet with various pressure ratios, and jet impingement on a surface were compared with analytical, numerical, and experimental solutions available in the literature. The dusty gas model was also validated with the experimental results [82] for the particle-laden underexpanded jet problem. It was shown that the relaxation zone behind the shock front and the pressure increment at the contact discontinuity which occur due to the presence of solid particles are perfectly resolved. Further, it was demonstrated that the upstream movement of the Mach disk as a result of the addition of dust particles is correctly predicted. A more detailed verification and validation for the specific problem of interest in this work is established in this section.

3.1.1 Grid independency study

A study on the grid-independency of solutions is presented in **Fig. 3**, where four different mesh sizes of h=1/4, 1/8, 1/16, and 1/32 are considered, with h being the characteristic size of the grid. The normalized profiles of pressure, density, temperature besides Mach number along the symmetry plane are compared for this analysis. A grid resolution with h=1/32 was found to provide results almost identical to h=1/64, and hence this grid was used for the rest of the simulations. The same grid was used for the multiphase cases as well. It is noteworthy that the selected grid does not resolve all the smaller-scale features of the flow, including a von Kármán vortex street type shedding of vortexlets. Such nearfield features will also be analyzed using a truncated domain with finer mesh sizes and will be discussed in the upcoming sections.

3.1.2 Validation of results with experimental results

In **Fig. 4**, the density isopycnics of the DG solution are compared with the experimental results (holographic interferograms) for five different recorded times (t = 28, 53, 102, 130, and 172 μs) in accordance with [15]. The figure demonstrates how the flow evolved during a course shorter than 0.2 ms. The step by step process is comprised of several distinguished phenomena: 1) shock impingement on the wedge and formation of a single Mach reflection, 2) passage of the incident shock and Mach stem over the wedge and formation of an expansion fan, 3) development of the primary vortex, 4) emerge of a slip line from the triple point into the vortex, 5) reflection of the Mach stem on the symmetry axis leading to the emanation of the reflected shock interacting with the vortex, and 6) formation of a second triple point and a new slip line. It should be noted that the reflected shock interacting with the vortex is split into an accelerated and a decelerated shock. The comparison, in **Fig. 4** (a) to (f), demonstrates there is a perfect qualitative agreement with the results of the experiments in space and time.

In **Fig. 5**, the numerical shadowgraphs of the pure gas model are compared with the experimental shadowgraphs of Chang and Chang [15] for different time steps. It can be observed that the basic flow structures, including the two split shocks after impingement on the vortex (one in and the other against the direction of vortex circulation), and the V-shaped decelerated deflected shock are nicely captured. The only feature which is not properly resolved in the numerical solutions is the vortexlets string emerging in the slip layer of the main vortex due to a Kelvin–Helmholtz instability. It should be noted that this feature can also be resolved if a finer grid or higher-order polynomials are applied. While the main purpose of the current work is to investigate the effect of the addition of dust particles on the overall (large-scale) structure of the flow, we have also covered the role of the addition of dust particles on the smaller-scale structures (vortexlets).

Fig. 6 investigates the details of the shock-vortex interaction in the vicinity of the wedge. To save computational cost, a smaller domain with a finer grid size is simulated, to highlight the smaller-scale features present in the flowfield. The same grid is then used to analyze how the addition of dust particles affects these flow structures. As mentioned earlier, the reflected shock, which is sucked towards the main vortex, is scattered into accelerating and decelerating shocks, as evident in the figure. In **Fig. 6**, one can also observe how, with the passage of the secondary slipstream, a series of vortexlets are shed alongside the slip layer of the main vortex which interacts with the discontinuities and disappears as time passes by. Further, the decelerated shock inside the vortex generates a transmitted shock. Subsequently, the interaction of the decelerated shock with the vortexlets leads to the emergence of diverging acoustics. The above-mentioned process is described in detail in **Fig. 6** (a) to (e) during the initial time steps of the formation of the flow.

3.2 Multiphase results

3.2.1 The effects of adding dust particles on wave patterns in Schardin's problem

Fig. 7 demonstrates the effects of adding particles to the flow. In the simulated test case, glass beads with a diameter of 10 μm and a microscopic density of 2,500 kg/m^3 were distributed uniformly in the whole domain. The particulate loading (β) was set equal to 10. In the figure, the top half of each slot is the pure gas solution, and the bottom half represents the dusty gas case. It can be seen that all the basic structures observed in the pure gas case are present in the dusty gas case as well; however, all the discontinuities are either decelerated or accelerated when dust particles are added. More specifically, the left running discontinuities, i.e., the reflected shock wave and rarefaction waves, are accelerated, while all the other right-running discontinuities including slip lines, incident, and accelerated shocks, are decelerated compared to the case of pure gas. When the incident shock wave passes by the seeded flowfield, the particles are accelerated by the drag force that the gas phase imposes on them. This leads to an increase of pressure and total pressure behind the incident shock wave; therefore, compared to the pure gas case, a larger pressure difference powers the reflected shock wave, which consequently translates into its acceleration. Some discrepancies between the pure gas case and dusty gas in the vicinity of the vortex become obvious as the particles are transferred from the vortex core towards the vortex edges. Moreover, as the intensity of the shadowgraph lines implies, in the dusty gas case, the discontinuities are more relaxed compared to the pure gas counterpart, as solid particles with non-negligible inertia cannot follow the abrupt changes in gas flow. The diameter, density, and heat capacity of the solid particles determine the size of this relaxation zone [47].

The accumulation of dust particles and the formation of a particle-free region in the center of the vortex are demonstrated in **Fig. 8**. The overlaid gas density contour lines on the concentration contours of the dust are shown for two particulate loadings in a zoomed view behind the prism. The dust particles are clearly convected towards the edge of the vortex and form a low-density region in the core of the vortex. The accumulation of the particles diminishes the slip layer and slip line. Moreover, the waves are not only decelerated but also attenuated. The larger the particulate loading, the more intensive the multiphase effects.

3.2.2 Parametric study of dust particles diameter

Fig. 9 illustrates the effects of varying particle diameter on some of the parameters, which describe the structure of the flow. Interestingly, at a certain particulate loading, as the diameter of the particles decreases, the coupling effects increase. Accordingly, dust particles can follow the gas phase more closely. Larger particles, on the other hand, have a shorter response time and therefore, the particle motion is largely defined by the carrier gas phase rather than its previous history. Because the drag force acting on the particles is proportional to the velocity difference between the phases, the carrier gas is less affected when seeded with larger particles. This can be observed in the normalized profiles of density, Mach and tangential velocity plotted alongside the symmetry line in **Fig. 9** (a) to (c). As time passes, the fine-grained dispersed phase deviates more from the gas phase.

For large diameter particles (50 and 100 μm), the trends are almost identical to that of the pure gas. However, when small diameter particles are added to the flowfield, the dynamics of the flow are completely different. As shown in the figure, for a particle diameter of 1 μm, the vortex region is not developed to the same extent as the other cases. Even the formation of some of the inherent features in Schardin's problem, including the accelerated shocks and the shear layer, are not observed. **Fig. 9** (d) represents the time transition of the locus of the vortex core. This location is plotted for three time-steps, demonstrating the increase in deviation of the small-sized dust diameter from pure gas with passing time. It can be seen that the downstream movement of the vortex locus is slowed down when particles are added to the flow. Again, the smaller the diameter of the particles, the slower the movement of the vortex locus.

3.2.3 Parametric study on particulate loading

Particulate loading manifests itself as the mass of particles in the formulation of the response time. The higher particulate loading corresponds to the longer response time of the particulate phase. The effect of increasing particulate loading is investigated in **Fig. 10**. For this analysis, particles with a diameter of 10 μm were selected and plots of various parameters alongside the symmetry plane for pure gas and particulate loadings of 1 and 10 are compared. It can be observed that increasing the particulate loading postpones the formation of shock-vortex structures, due to more pronounced coupling effects between the carrier phase and solid grains. As can be seen in **Fig. 10** (d), in a flow with a larger particulate loading, the vortex is convected towards the reflected shock at a slower pace. The reflected shock is also more attenuated as the particulate loading is increased. The superposition of these effects leads to a very weak shock-vortex in which many of the innate patterns of the pure gas case are predominantly altered. Some of these changes include the disappearance of the accelerated shock in density and Mach profiles, as well as the disappearance of the slip layer effect in tangential velocity. These effects can be observed in **Fig. 10** (a) to (c).

3.2.4 On the role of dust on noise generation in shock-vortex interaction

A crucial parameter which can shed light on the time evolution of the vorticity is the area-weighted enstrophy, defined as [23]

$$En(t) = \int_{\partial A} \Omega_z^2 \left(x, y, t \right) dxdy \, , \tag{18}$$

in which Ω is the vorticity of the compressible gases as follows

$$\Omega_z = \frac{\partial v}{\partial x} - \frac{\partial u}{\partial y} \, . \tag{19}$$

In **Fig. 11**, the enstrophy plots for two different particulate loadings and four different particle diameters are plotted with respect to time. This analysis provides a better understanding of how the dust particles can affect the strength of the incident shock via attenuation, and hence affect the strength of the primary vortex as well as vortexlets. The enstrophy profiles soar at t=30 μs. This is when the primary vortex is being formed. The profiles reach a maximum just a little before t=100 μs. Then, depending on the diameter size and the particulate loading of the simulated case, two different trends may be observed: 1) A slight decrease followed by a slight increase and 2) a slight monotone decrease. The smaller the particle diameters and the higher the particulate loadings, the larger the decay of vorticity. As time passes (t>100 μs), the formation of vortexlets in the slip layer induces a slight increase in enstrophy magnitude.

The addition of particles is, however, acting in the opposite direction. It is clear that particles tend to decay the vorticities. For the higher particulate loading case simulated here with a particle diameter size of 1 μm, the effect is so potent that even the primary vortex is not formed in the time considered. In the following subsection, when the effects of added dust particles on the behavior of smaller-scale vortexlet are investigated via plots of streamlines, these explanations will be justified.

3.2.5 On the role of dust on the decay of the vortexlets

In the following figures, we aim to analyze the role of the addition of dust particles on smaller-scale structures observed in the vicinity of the wedge. **Fig. 12** shows the time transition of the gas density isopycnics when dust particles with different diameters are added to the flowfield. Here, the particulate loading is set equal to 1. The level of interaction of gas and particles depends on the Stokes number, which is defined as the ratio of the relaxation time of the particles to the time scale of the fluid flow [83],

$$St = \frac{\tau_V}{t_{ref}}. \tag{20}$$

Here t_{ref} is a reference time which can be defined as the characteristic length divided by the characteristic speed, and τ_V is the momentum (velocity) response time of the particles given by [83]

$$\tau_V = \frac{\rho_s d^2}{18\mu_g}. \tag{21}$$

A summary of the important parameters in gas-particle flows is provided in **Table 4**. It can be observed that the coupling effects gain significance as the diameter of the particles decrease. This is due to the fact that smaller particle diameters lead to flows with a smaller Stokes number. For very small diameter particles (St<<1), the particulate phase will be in dynamic equilibrium with the career phase. Therefore particles will closely follow the streamlines of the vortical flow.

On the other hand, large particles (*St*>>1) will be unaffected by the vortices of the fluid flow due to large inertia. There may be an intermediate case where intermediate particle sizes (*St*≈1) will be centrifuged from the vortex cores and accumulate at the edge of the vortices, leading to inhomogeneous particle concentrations. The follow-up and accumulation of particles on the vortex edge leads to the decay of these structures. However, it should be noted that the accumulation of particles in the core of the main vortex is much more effective than the small vortexlets. As **Fig. 13** demonstrates, these effects are amplified by increasing the particulate loading. Comparison of **Fig. 12** and **Fig. 13** reveals that when β=1, the addition of particles with diameters larger than 10 μm has an almost negligible effect. However, as the particulate loading increases, particles as large as 50 μm can slightly affect the structure of the flowfield. For β=10 and particle diameters smaller than 50 μm, the coupling effects are significant.

4 Conclusions

The primary motivations for this study were the importance of the shock-vortex interaction problem, the potential for this phenomenon occurring in a dusty environment, and the lack of an analysis that considers this triple interaction. Here, the Schardin's problem in a dusty environment was analyzed numerically using a modal discontinuous Galerkin method. Applying a DG method in the simulation of dusty gas flows with the presence of discontinuities is beneficial in many ways. A case in point is when resolving the flow features requires a very fine grid, but the size of the particles limits the computational grid size.

Cases covering a wide range of particle diameters with two different particulate loadings were simulated and the results were discussed in terms of isopycnics, shadowgraphs and profiles. Regarding the interaction of shocks with dust, it was observed that while the incident shock and other discontinuities are decelerated, the reflected left-running shock is accelerated in a dusty environment. It is also worth noting that the initial condition of the dust seeded in the domain affects the strength of the shock in the first place. The attenuated incident shock can, however, produce a vortex behind the wedge. The case of β=10 and d=1 μm was the only exception among present numerical experiments where no vortex can emerge.

It was shown that as the particle diameter became smaller, the effects became more potent. Moreover, increasing the particulate loading magnifies the effects. **Table 5** wraps up the step by step process of formation of different features which appear in the Schardin's and dusty Schardin's problems.

We have further demonstrated that the downstream movement of the primary vortex takes place at a slower pace when dust particles are added. This is partially due to interaction with the particles, and the drag force which is imposed on the core. The other factor is the attenuation of the initial incident shock which itself is caused by the presence of dust particles. The enstrophy profiles can also provide essential information regarding the flow evolution over time, and the role of dust on damping the instabilities. The formation of a dust-free region in the core of the vortex and a concentrated region on the edge of the vortex was also demonstrated.

In the current work, regardless of the validity of the mathematical model in the regime investigated, we applied a dusty gas model equation. In future work, we aim to focus on the so-called *granular flow* regime when the particle-particle or wall-particle interactions are more dominant compared to the interstitial forces. Considering other variants of the problem with different dust initialization is also a topic of interest that will be pursued in future works.

Acknowledgment

This work was supported by the National Research Foundation of Korea (NRF 2017-R1A5A1015311), South Korea. The first author (O.E.) acknowledges the support provided by the institutional research program (K19L03C06) from the Korea Institute of Science and Technology Information (KISTI), South Korea. The first author (O.E.) and the second author (A.R.) have contributed to this work equally.

References

[1] S. Pao, J. Seiner, Shock-associated noise in supersonic jets, AIAA Journal, 21 (1983) 687-693.
[2] H.S. Ribner, Cylindrical sound wave generated by shock-vortex interaction, AIAA Journal, 23 (1985) 1708-1715.
[3] P. Lu, K. Wu, On the shock enhancement of confined supersonic mixing flows, Physics of Fluids A: Fluid Dynamics, 3 (1991) 3046-3062.
[4] L. Guichard, L. Vervisch, P. Domingo, Two-dimensional weak shock-vortex interaction in a mixing zone, AIAA Journal, 33 (1995) 1797-1802.
[5] M. Smart, I. Kalkhoran, S. Popovic, Some aspects of streamwise vortex behavior during oblique shock wave/vortex interaction, Shock Waves, 8 (1998) 243-255.
[6] W. Hollingsworth, A schlieren study of the interaction between a vortex and a shock wave in a shock tube, British Aeronaut. Research Council Rept. 17,985, (1955).
[7] D.S. Dosanjh, T.M. Weeks, Interaction of a starting vortex as well as a vortex street with a traveling shock wave, AIAA Journal, 3 (1965) 216-223.
[8] J.L. Ellzey, M.R. Henneke, J.M. Picone, E.S. Oran, The interaction of a shock with a vortex: shock distortion and the production of acoustic waves, Physics of Fluids, 7 (1995) 172-184.

[9] T.M. Weeks, d.S. Dosanjh, Sound generation by shock-vortex interaction, AIAA Journal, 5 (1967) 660-669.
[10] O. Inoue, Y. Hattori, Sound generation by shock–vortex interactions, Journal of Fluid Mechanics, 380 (1999) 81-116.
[11] S. Sivier, E. Loth, J. Baum, R. Löhner, Vorticity produced by shock wave diffraction, Shock Waves, 2 (1992) 31-41.
[12] S.K. Lele, Compact finite difference schemes with spectral-like resolution, Journal of Computational Physics, 103 (1992) 16-42.
[13] S. Zhang, Y.-T. Zhang, C.-W. Shu, Multistage interaction of a shock wave and a strong vortex, Physics of Fluids, 17 (2005) 116101.
[14] K. Meadows, D. Caughey, The roles of shock motion and deformation in generation of shock noise, AIAA Paper 96-1777, 1996.
[15] S.M. Chang, K.S. Chang, On the shock–vortex interaction in Schardin's problem, Shock Waves, 10 (2000) 333-343.
[16] S.M. Chang, K.S. Chang, Visualization of shock-vortex interaction radiating acoustic waves, Journal of Visualization, 3 (2000) 221-228.
[17] A. Chatterjee, S. Vijayaraj, Multiple sound generation in interaction of shock wave with strong vortex, AIAA Journal, 46 (2008) 2558-2567.
[18] P. Halder, S. De, K. Sinhamahapatra, N. Singh, Numerical simulation of shock–vortex interaction in Schardin's problem, Shock Waves, 23 (2013) 495-504.
[19] A. Rault, G. Chiavassa, R. Donat, Shock-vortex interactions at high Mach numbers, Journal of Scientific Computing, 19 (2003) 347-371.
[20] H. Xiao, R.S. Myong, Computational simulations of microscale shock–vortex interaction using a mixed discontinuous Galerkin method, Computers & Fluids, 105 (2014) 179-193.
[21] S. Singh, A. Karchani, R.S. Myong, Non-equilibrium effects of diatomic and polyatomic gases on the shock-vortex interaction based on the second-order constitutive model of the Boltzmann-Curtiss equation, Physics of Fluids, 30 (2018) 016109.
[22] H. Schardin, High frequency cinematography in the shock tube, The Journal of Photographic Science, 5 (1957) 17-19.
[23] K. Koffi, Y. Andreopoulos, C.B. Watkins, Dynamics of microscale shock/vortex interaction, Physics of Fluids, 20 (2008) 126102.
[24] O. Igra, G. Ben-Dor, Z. Rakib, The effect of dust and water droplets on the relaxation zone developed behind strong normal shock waves, International Journal of Multiphase Flow, 11 (1985) 121-132.
[25] G. Lock, Experimental measurements in a dusty-gas shock tube, International Journal of Multiphase Flow, 20 (1994) 81-98.
[26] G. Ben-Dor, Dust entrainment by means of a planar shock induced vortex over loose dust layers, Shock Waves, 4 (1995) 285-288.
[27] A. Levy, Shock waves interaction with granular materials, Powder Technology, 103 (1999) 212-219.
[28] T. Saito, Numerical analysis of dusty-gas flows, Journal of Computational Physics, 176 (2002) 129-144.
[29] O. Igra, G. Hu, J. Falcovitz, B. Wang, Shock wave reflection from a wedge in a dusty gas, International Journal of Multiphase Flow, 30 (2004) 1139-1169.
[30] H. Liu, Y. Guo, W. Lin, Simulation of shock-powder interaction using kinetic theory of granular flow, Powder Technology, 273 (2015) 133-144.
[31] A. Rahimi, O. Ejtehadi, K.H. Lee, R.S. Myong, Near-field plume-surface interaction and regolith erosion and dispersal during the lunar landing, Acta Astronautica, 175 (2020) 308-326.
[32] P. Saffman, On the stability of laminar flow of a dusty gas, Journal of Fluid Mechanics, 13 (1962) 120-128.
[33] B. Lazaro, J. Lasheras, Particle dispersion in a turbulent, plane, free shear layer, Physics of Fluids A: Fluid Dynamics, 1 (1989) 1035-1044.
[34] A. Volkov, Y.M. Tsirkunov, B. Oesterle, Numerical simulation of a supersonic gas–solid flow over a blunt body: The role of inter-particle collisions and two-way coupling effects, International Journal of Multiphase Flow, 31 (2005) 1244-1275.

[35] Y. Huang, W. Wu, H. Zhang, Numerical study of particle dispersion in the wake of gas-particle flows past a circular cylinder using discrete vortex method, Powder Technology, 162 (2006) 73-81.
[36] T. Uchiyama, S. Shimada, Numerical simulation of the interactions between a vortex pair and solid particles near a wall, Powder technology, 257 (2014) 55-67.
[37] F. Bambauer, S. Wirtz, V. Scherer, H. Bartusch, Transient DEM-CFD simulation of solid and fluid flow in a three dimensional blast furnace model, Powder Technology, 334 (2018) 53-64.
[38] L. Li, H. Qi, Z. Yin, D. Li, Z. Zhu, V. Tangwarodomnukun, D. Tan, Investigation on the multiphase sink vortex Ekman pumping effects by CFD-DEM coupling method, Powder Technology, 360 (2020) 462-480.
[39] T. Uchiyama, H. Yagami, Numerical simulation for the collision between a vortex ring and solid particles, Powder Technology, 188 (2008) 73-80.
[40] J. Xu, J. Zhang, H. Wang, J. Mi, Fine Particle Behavior in the Air Flow Past a Triangular Cylinder, Aerosol Science and Technology, 47 (2013) 875-884.
[41] S.S. Tiwari, E. Pal, S. Bale, N. Minocha, A.W. Patwardhan, K. Nandakumar, J.B. Joshi, Flow past a single stationary sphere, 1. Experimental and numerical techniques, Powder Technology, (2019).
[42] O. Ejtehadi, R.S. Myong, Eulerian-Eulerian simulation of dusty gas flows past a prism from subsonic to supersonic regimes using a modal discontinuous Galerkin method, In Review.
[43] M. Afkhami, A. Hassanpour, M. Fairweather, Effect of Reynolds number on particle interaction and agglomeration in turbulent channel flow, Powder Technology, 343 (2019) 908-920.
[44] C.T. Crowe, T.R. Troutt, J.N. Chung, Particle Interactions with Vortices, in: S.I. Green (Ed.) Fluid Vortices, Springer Netherlands, Dordrecht, 1995, pp. 829-861.
[45] A. Fedorov, Y.V. Kharlamova, T.A. Khmel, Reflection of a shock wave in a dusty cloud, Combustion, Explosion, and Shock Waves, 43 (2007) 104-113.
[46] C.G. Ilea, P. Kosinski, A.C. Hoffmann, The effect of polydispersity on dust lifting behind shock waves, Powder Technology, 196 (2009) 194-201.
[47] O. Ejtehadi, A. Rahimi, A. Karchani, R.S. Myong, Complex wave patterns in dilute gas–particle flows based on a novel discontinuous Galerkin scheme, International Journal of Multiphase Flow, 104 (2018) 125-151.
[48] B. Cockburn, G.E. Karniadakis, C.W. Shu, Chapter 1: The development of discontinuous Galerkin methods, Discontinuous Galerkin Methods, Springer, 2000.
[49] E. Franquet, V. Perrier, Runge–Kutta discontinuous Galerkin method for the approximation of Baer and Nunziato type multiphase models, Journal of Computational Physics, 231 (2012) 4096-4141.
[50] M. Owkes, O. Desjardins, A discontinuous Galerkin conservative level set scheme for interface capturing in multiphase flows, Journal of Computational Physics, 249 (2013) 275-302.
[51] H. Lu, J. Zhu, D. Wang, N. Zhao, Runge–Kutta discontinuous Galerkin method with front tracking method for solving the compressible two-medium flow, Computers & Fluids, 126 (2016) 1-11.
[52] J. Moortgat, A. Firoozabadi, Mixed-hybrid and vertex-discontinuous-Galerkin finite element modeling of multiphase compositional flow on 3D unstructured grids, Journal of Computational Physics, 315 (2016) 476-500.
[53] O. Ejtehadi, R.S. Myong, A modal discontinuous Galerkin method for simulating dusty and granular gas flows in thermal non-equilibrium in the Eulerian framework, Journal of Computational Physics, 411 (2020) 109410.
[54] M.H. Ahmadian, E. Roohi, A. Teymourtash, S. Stefanov, A dusty gas model-direct simulation Monte Carlo algorithm to simulate flow in micro-porous media, Physics of Fluids, 31 (2019) 062007.
[55] B. Xiao, S. Wang, Y. Wang, G. Jiang, Y. Zhang, H. Chen, M. Liang, G. Long, X. Chen, Effective thermal conductivity of porous media with roughened surfaces by fractal-Monte Carlo simulations, Fractals, 28 (2020) 2050029.
[56] B. Xiao, W. Wang, X. Zhang, G. Long, J. Fan, H. Chen, L. Deng, A novel fractal solution for permeability and Kozeny-Carman constant of fibrous porous media made up of solid particles and porous fibers, Powder Technology, 349 (2019) 92-98.
[57] G. Long, S. Liu, G. Xu, S.-W. Wong, H. Chen, B. Xiao, A perforation-erosion model for hydraulic-fracturing applications, SPE Production & Operations, 33 (2018) 770-783.

[58] R. Ishii, Y. Umeda, M. Yuhi, Numerical analysis of gas-particle two-phase flows, Journal of Fluid Mechanics, 203 (1989) 475-515.
[59] S.W. Kim, K.S. Chang, Reflection of shock wave from a compression corner in a particle-laden gas region, Shock Waves, 1 (1991) 65-73.
[60] J.T. Jenkins, S.B. Savage, A theory for the rapid flow of identical, smooth, nearly elastic, spherical particles, Journal of Fluid Mechanics, 130 (1983) 187-202.
[61] C. Lun, S.B. Savage, D. Jeffrey, N. Chepurniy, Kinetic theories for granular flow: inelastic particles in Couette flow and slightly inelastic particles in a general flowfield, Journal of Fluid Mechanics, 140 (1984) 223-256.
[62] M. Reeks, On the constitutive relations for dispersed particles in nonuniform flows. I: Dispersion in a simple shear flow, Physics of Fluids A: Fluid Dynamics, 5 (1993) 750-761.
[63] D. Gidaspow, Multiphase Flow and Fluidization: Continuum and Kinetic Theory Descriptions, Academic Press, 1994.
[64] Y. Zhang, J.M. Reese, Particle–gas turbulence interactions in a kinetic theory approach to granular flows, International Journal of Multiphase Flow, 27 (2001) 1945-1964.
[65] R.W. Houim, E.S. Oran, A multiphase model for compressible granular–gaseous flows: formulation and initial tests, Journal of Fluid Mechanics, 789 (2016) 166-220.
[66] A. Busch, S.T. Johansen, On the validity of the two-fluid-KTGF approach for dense gravity-driven granular flows, Powder Technology, (2020).
[67] H. Miura, I.I. Glass, On a dusty-gas shock tube, Proceedings of the Royal Society of London A: Mathematical, Physical and Engineering Sciences, The Royal Society, 1982, pp. 373-388.
[68] F. Dobran, A. Neri, G. Macedonio, Numerical simulation of collapsing volcanic columns, Journal of Geophysical Research: Solid Earth, 98 (1993) 4231-4259.
[69] S.S. Tiwari, E. Pal, S. Bale, N. Minocha, A.W. Patwardhan, K. Nandakumar, J.B. Joshi, Flow past a single stationary sphere, 2. Regime mapping and effect of external disturbances, Powder Technology, (2019).
[70] X. Zhang, C.W. Shu, Positivity-preserving high order discontinuous Galerkin schemes for compressible Euler equations with source terms, Journal of Computational Physics, 230 (2011) 1238-1248.
[71] X. Zhang, C.W. Shu, On maximum-principle-satisfying high order schemes for scalar conservation laws, Journal of Computational Physics, 229 (2010) 3091-3120.
[72] T.J. Barth, D.C. Jespersen, The design and application of upwind schemes on unstructured meshes, AIAA Paper 89-0366, 1989.
[73] V.V. Rusanov, Calculation of Interaction of Non-steady Shock Waves with Obstacles, National Research Council Canada, Division of Mechanical Engineering, 1962.
[74] H. Nishikawa, K. Kitamura, Very simple, carbuncle-free, boundary-layer-resolving, rotated-hybrid Riemann solvers, Journal of Computational Physics, 227 (2008) 2560-2581.
[75] M.S. Liou, C.J. Steffen Jr, A new flux splitting scheme, Journal of Computational Physics, 107 (1993) 23-39.
[76] M.S. Liou, A sequel to AUSM, Part II: AUSM+-up for all speeds, Journal of Computational Physics, 214 (2006) 137-170.
[77] R. Saurel, E. Daniel, J.C. Loraud, Two-phase flows: Second-order schemes and boundary conditions, AIAA Journal, 32 (1994) 1214-1221.
[78] E. Toro, Riemann-problem-based techniques for computing reactive two-phased flows, Numerical Combustion, Springer, 1989.
[79] L. Sainsaulieu, Finite volume approximation of two phase-fluid flows based on an approximate Roe-type Riemann solver, Journal of Computational Physics, 121 (1995) 1-28.
[80] R. Saurel, R. Abgrall, A multiphase Godunov method for compressible multifluid and multiphase flows, Journal of Computational Physics, 150 (1999) 425-467.
[81] O. Ejtehadi, A. Rahimi, R.S. Myong, Numerical investigation of the counter-intuitive behavior of Mach disk movement in underexpanded gas-particle jets, Journal of Computational Fluid Engineering, 24 (2019) 19-28.
[82] M. Sommerfeld, The structure of particle-laden, underexpanded free jets, Shock Waves, 3 (1994) 299-311.
[83] C.T. Crowe, Multiphase Flow Handbook, CRC Press, 2005.

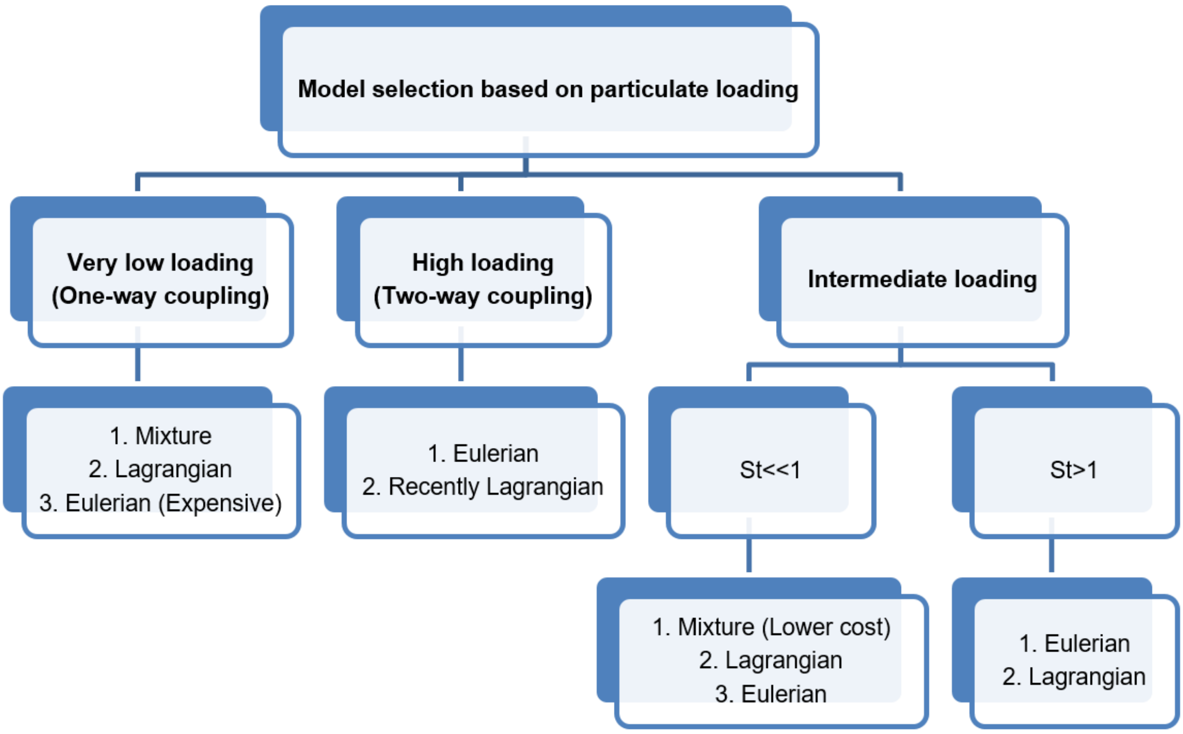

Fig. 1 Efficient mathematical models based on the level of phase coupling

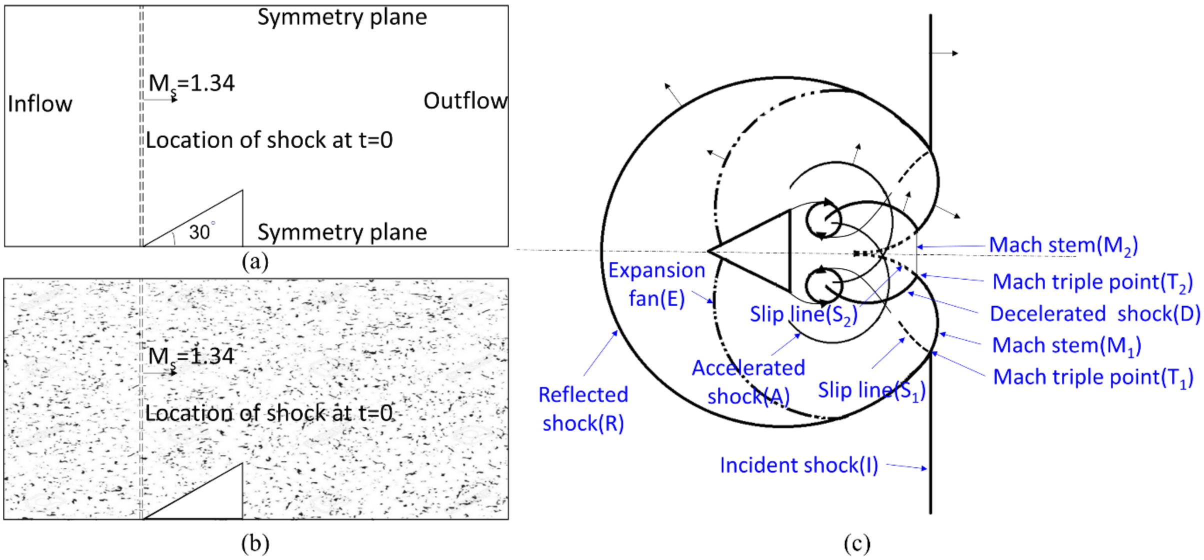

Fig. 2 Schematic of the initial and boundary conditions for (a) pure gas, (b) two-phase simulation, and (c) compressible flow elements present in Schardin's problem

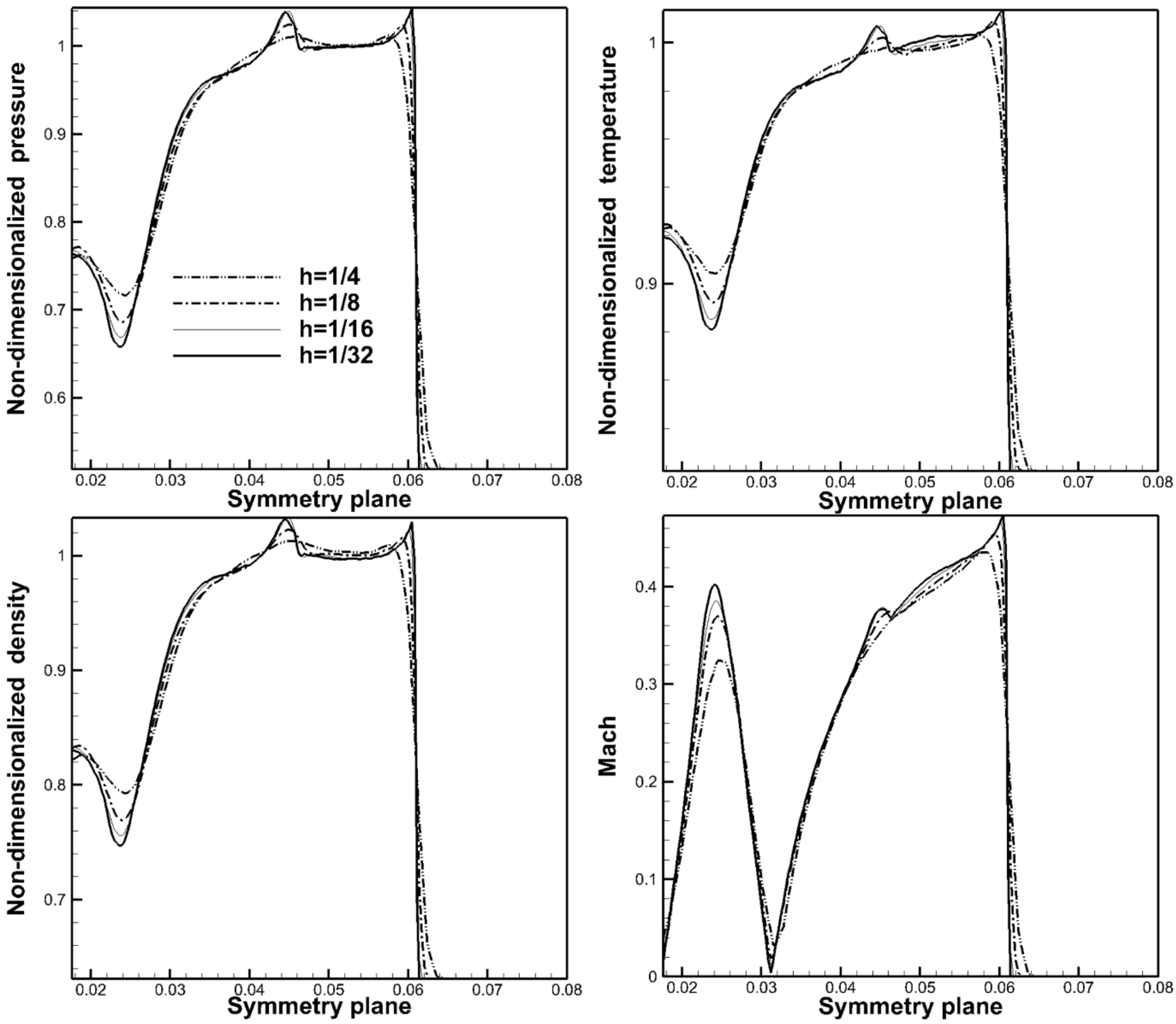

Fig. 3 Verification of the developed solver: Grid independency test: t=140 μs

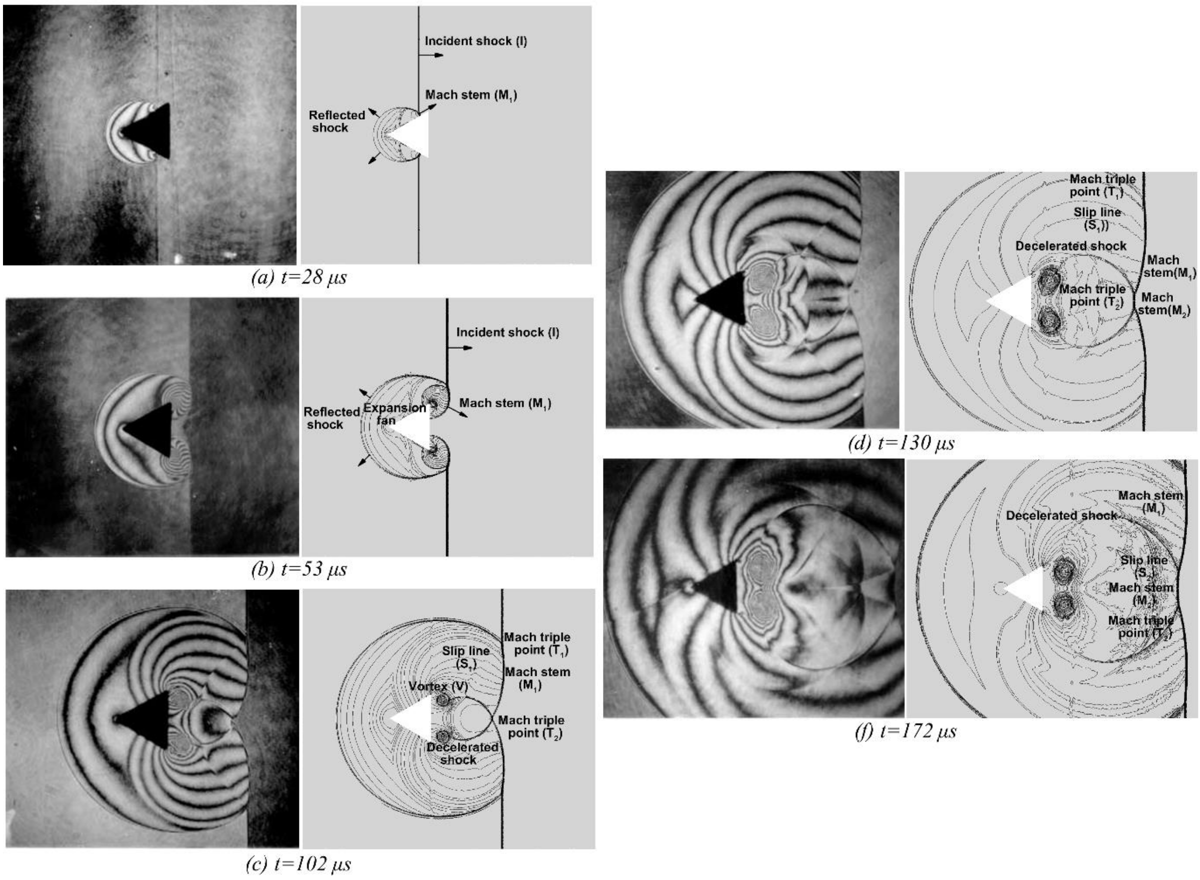

Fig. 4 Validation: Comparison of density solutions (right) with experimental data from Chang and Chang [13] (left)

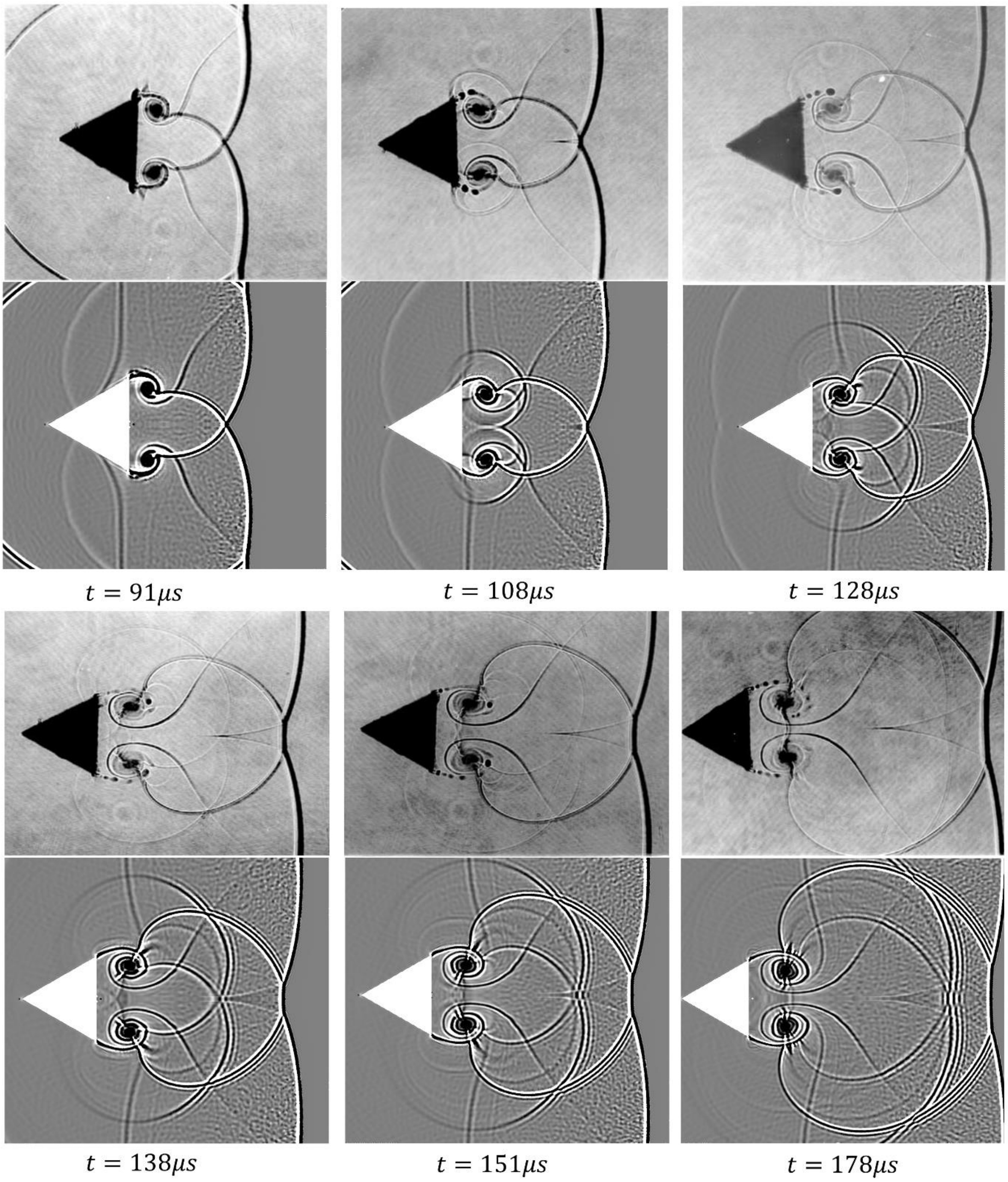

Fig. 5 Comparison of the numerical Schlieren photos (bottom) with experimental data from Chang and Chang [13] (top)

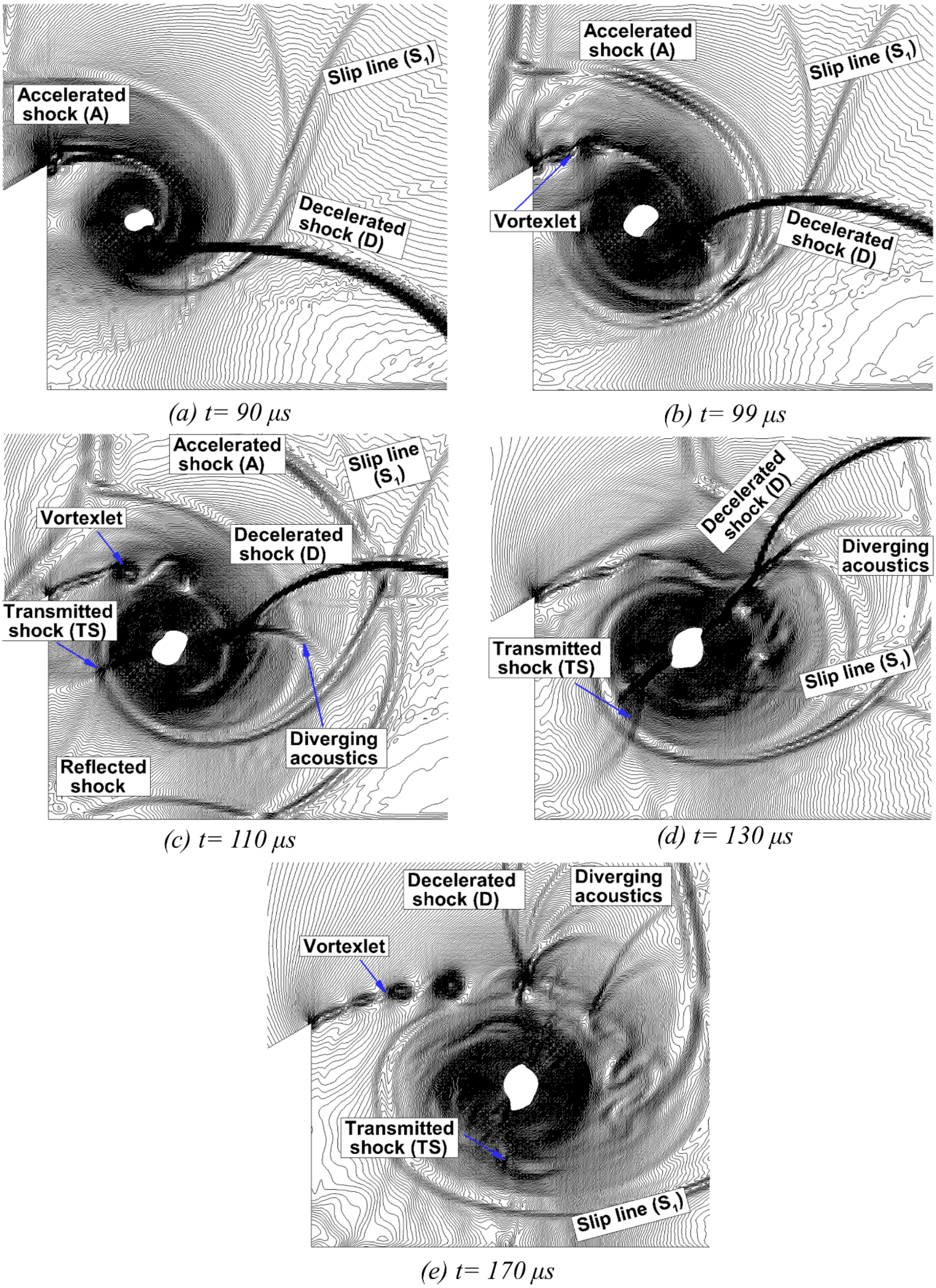

Fig. 6 Detailed analysis of time evolution of shock-vortex interaction: density isopycnics

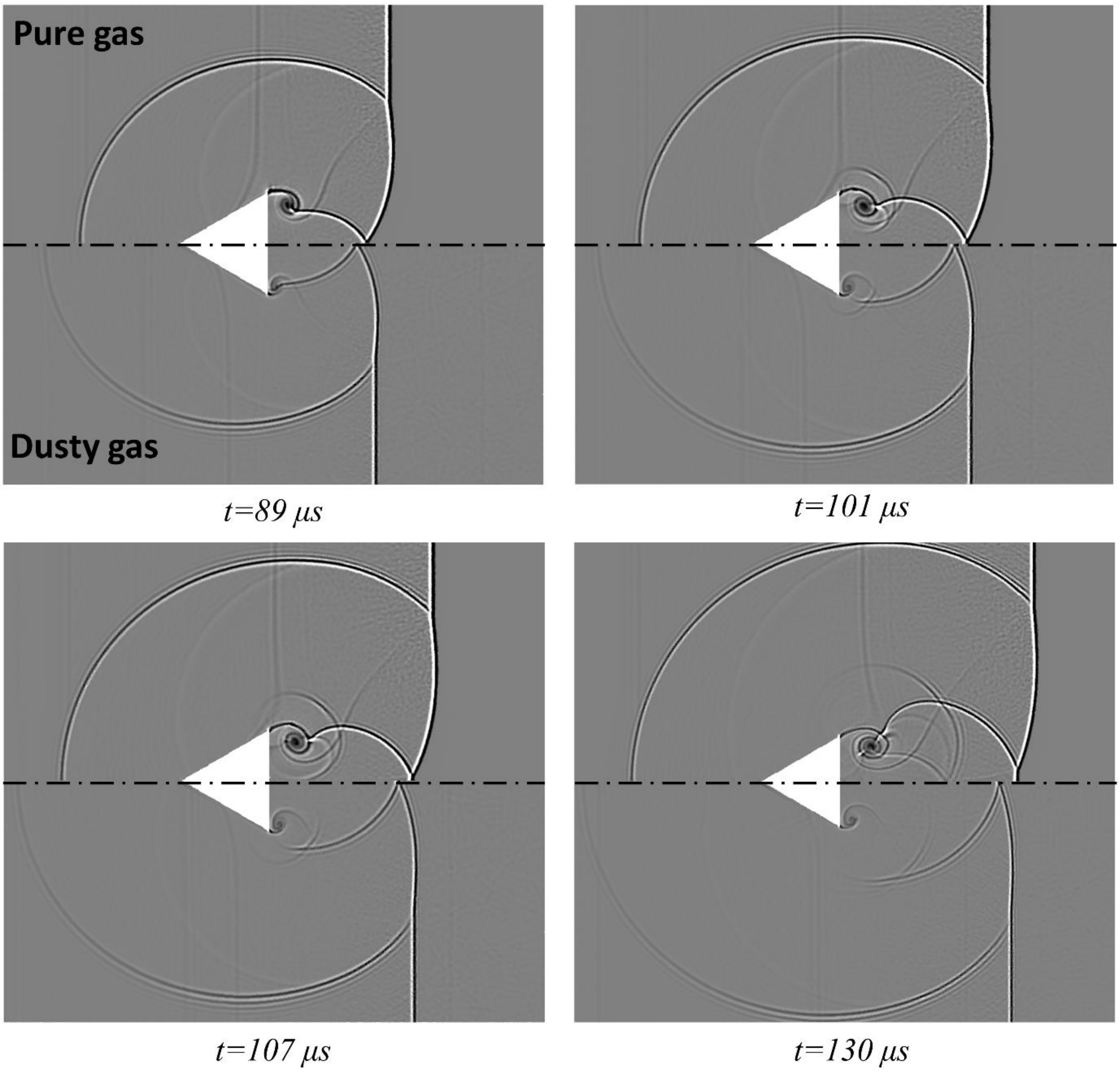

Fig. 7 Time evolution of numerical shadowgraphs; pure gas (top half) compared with dusty gas (bottom half) (d=10 μm, β=10)

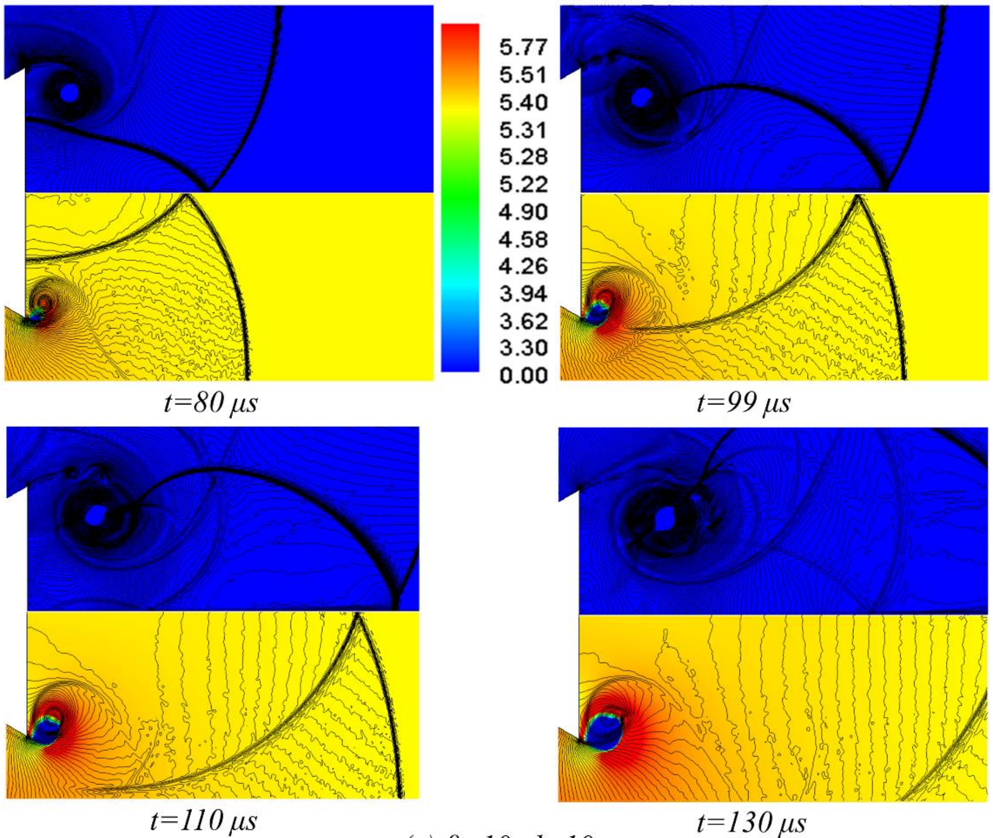

(a) β=10, d=10

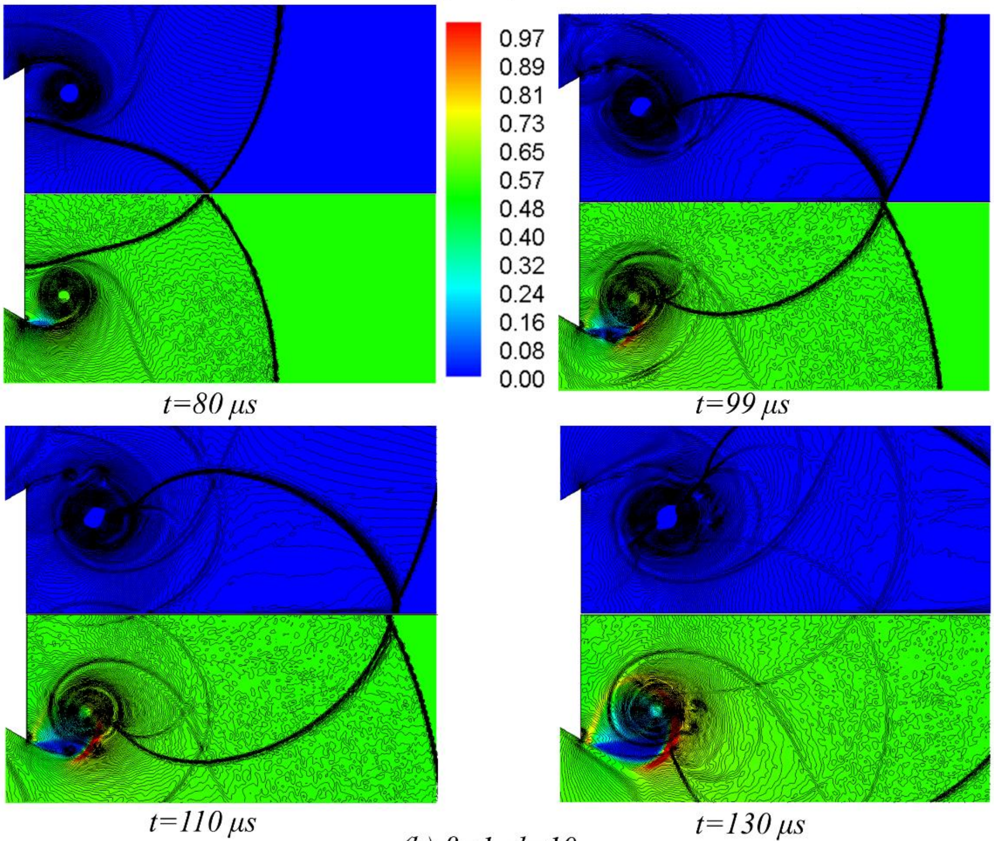

(b) β=1, d=10

Fig. 8 Comparison of gas density contour lines overlaid on dust phase contours for pure gas (top half) and dusty gas (bottom half)

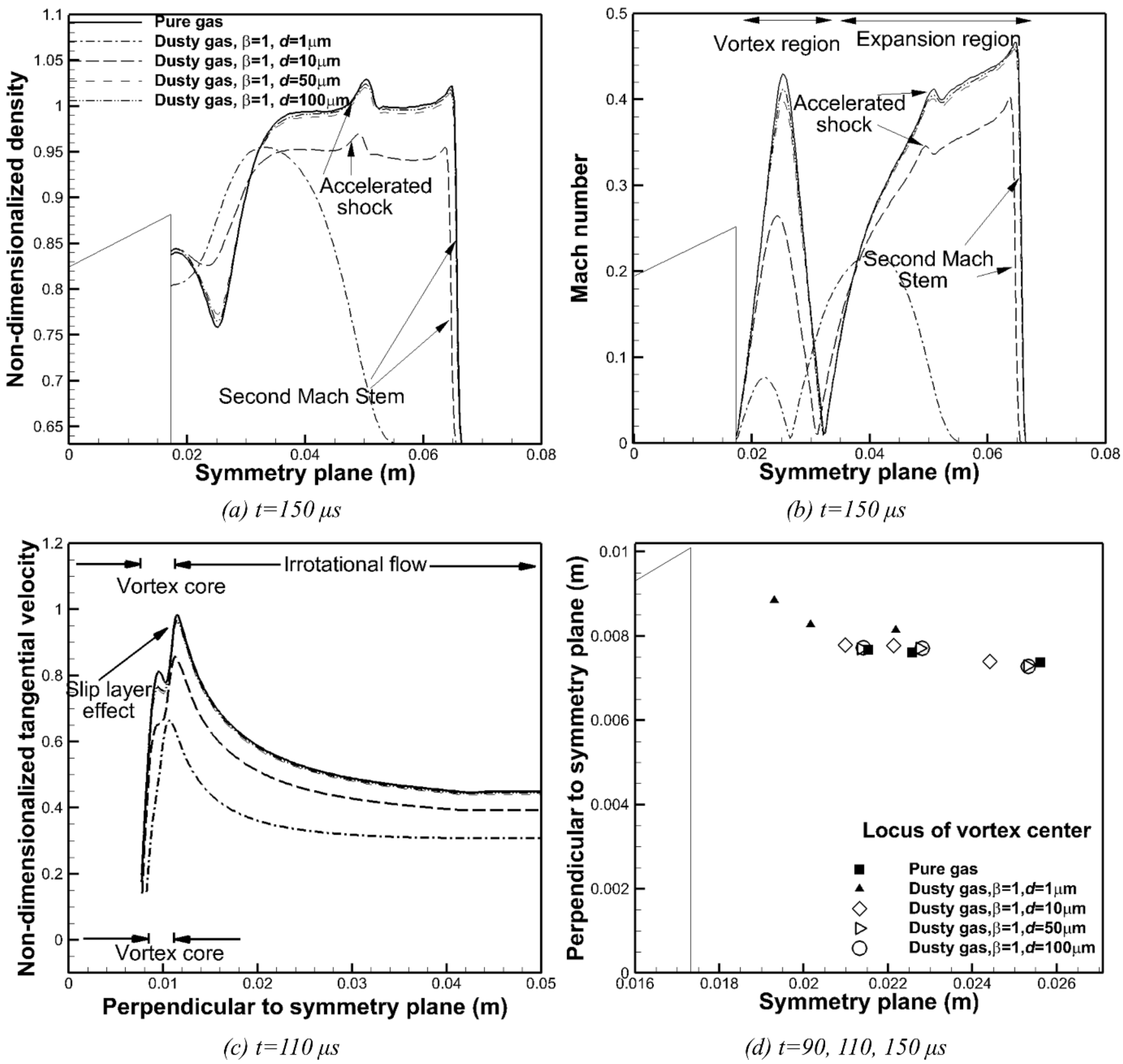

Fig. 9 Effect of particle diameter on the structure of the flow, β=1

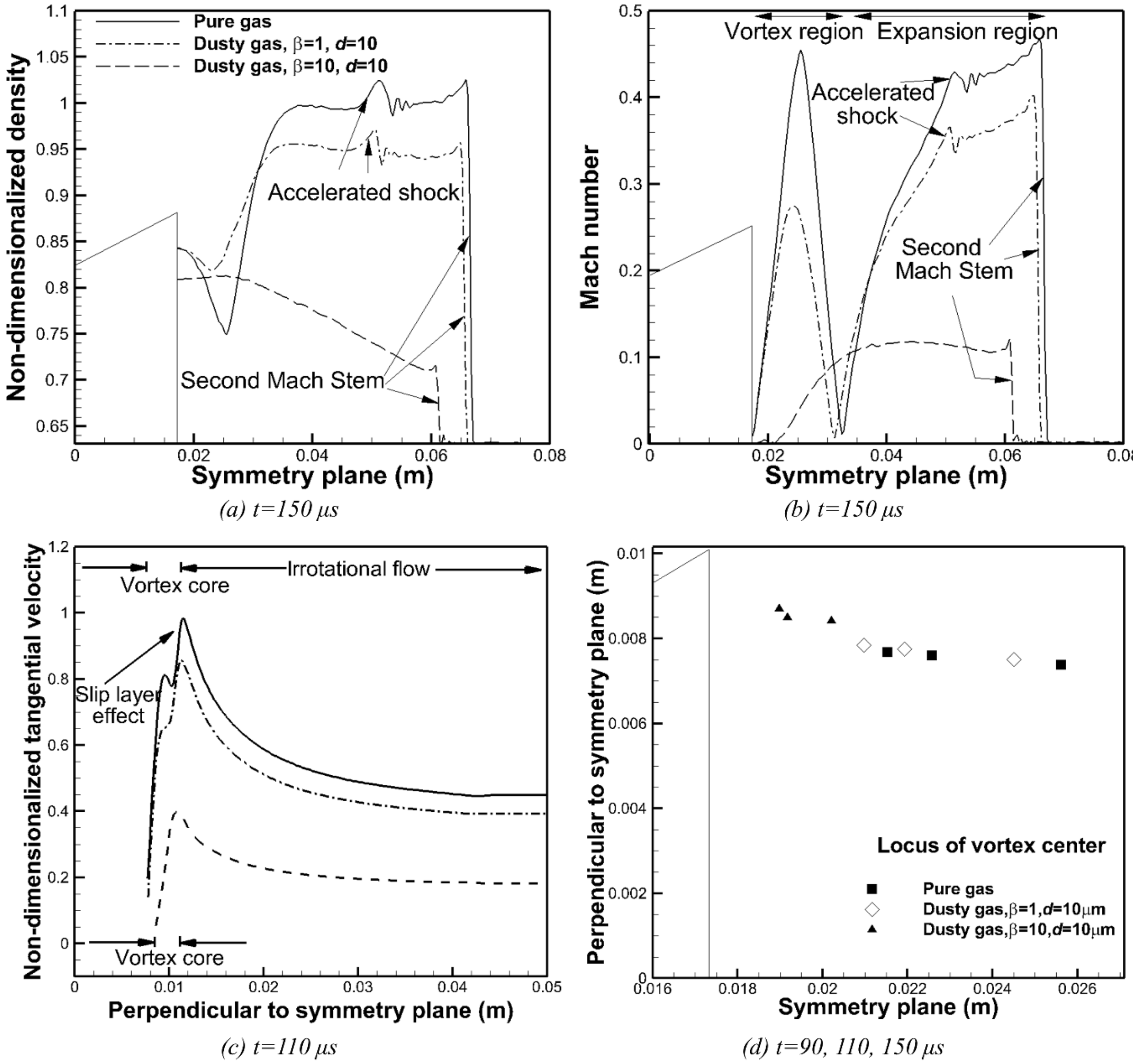

Fig. 10 Effect of particulate loading on the structure of the flow

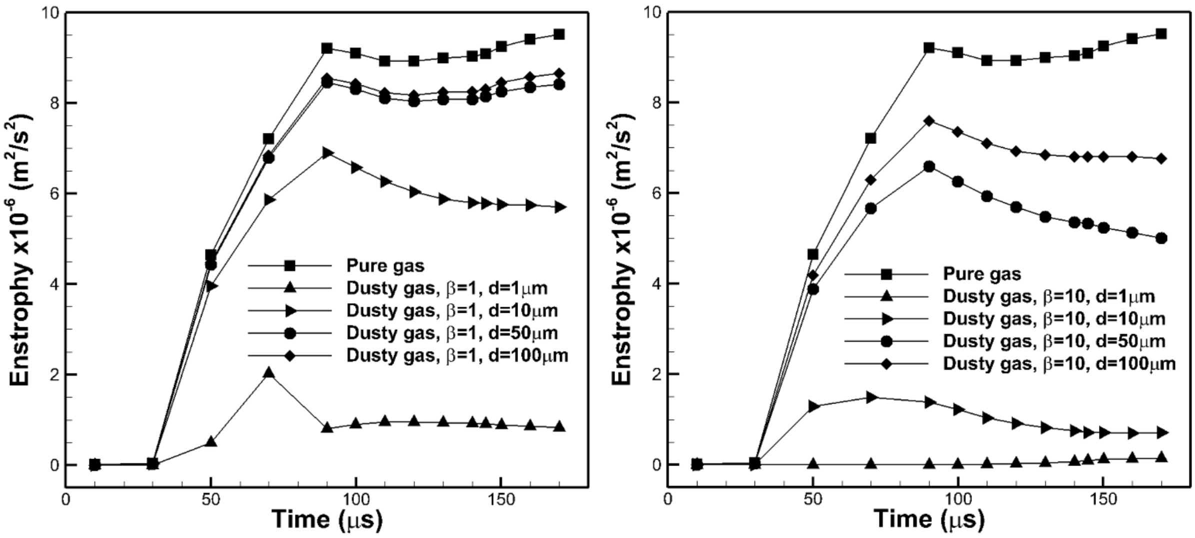

Fig. 11 Enstrophy plots for various particle diameter test cases (Left: β=1, Right: β=10)

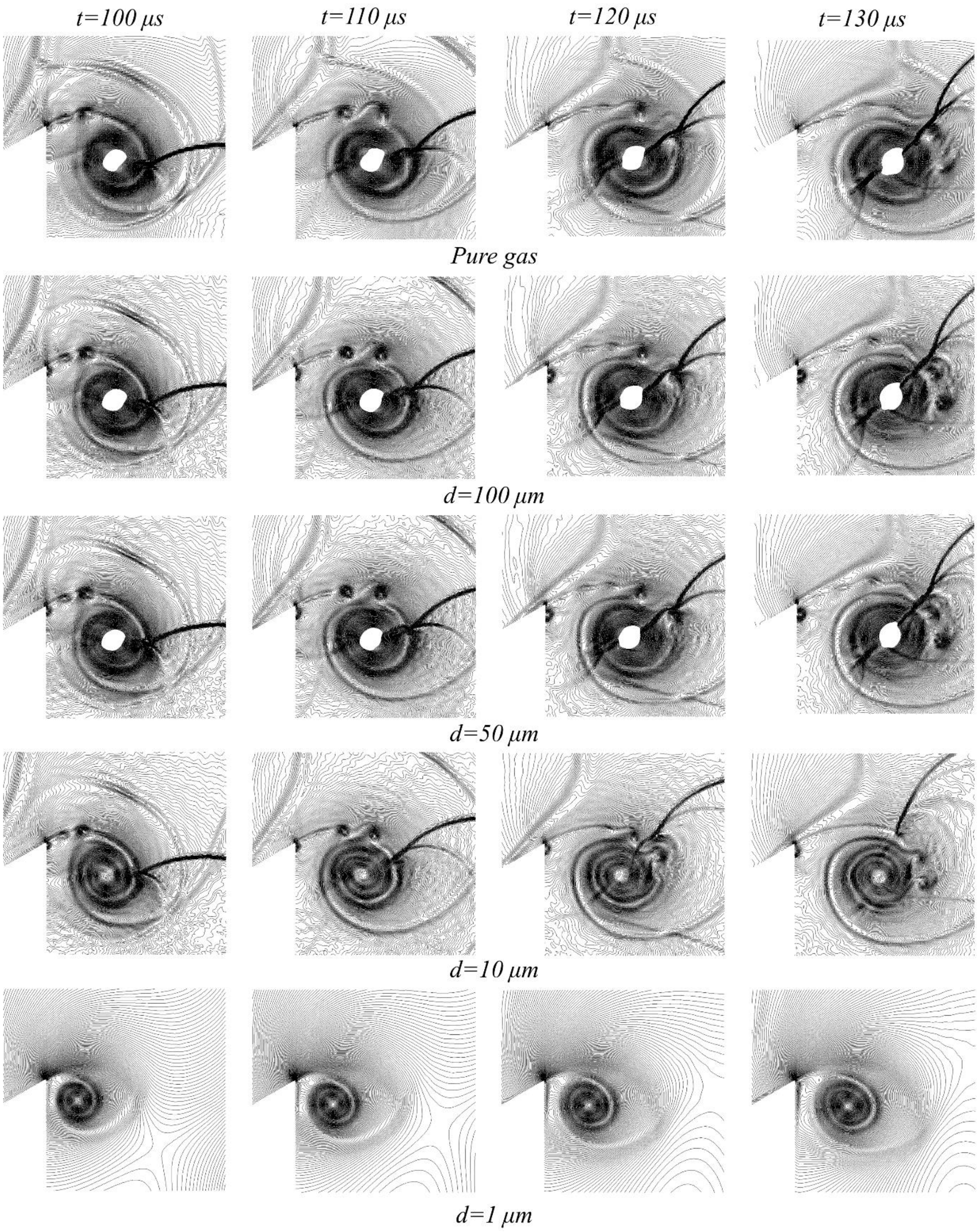

Fig. 12 Visualizing the effects of the addition different diameter size particles on the decay of vortexlets using density isopycnics β=1

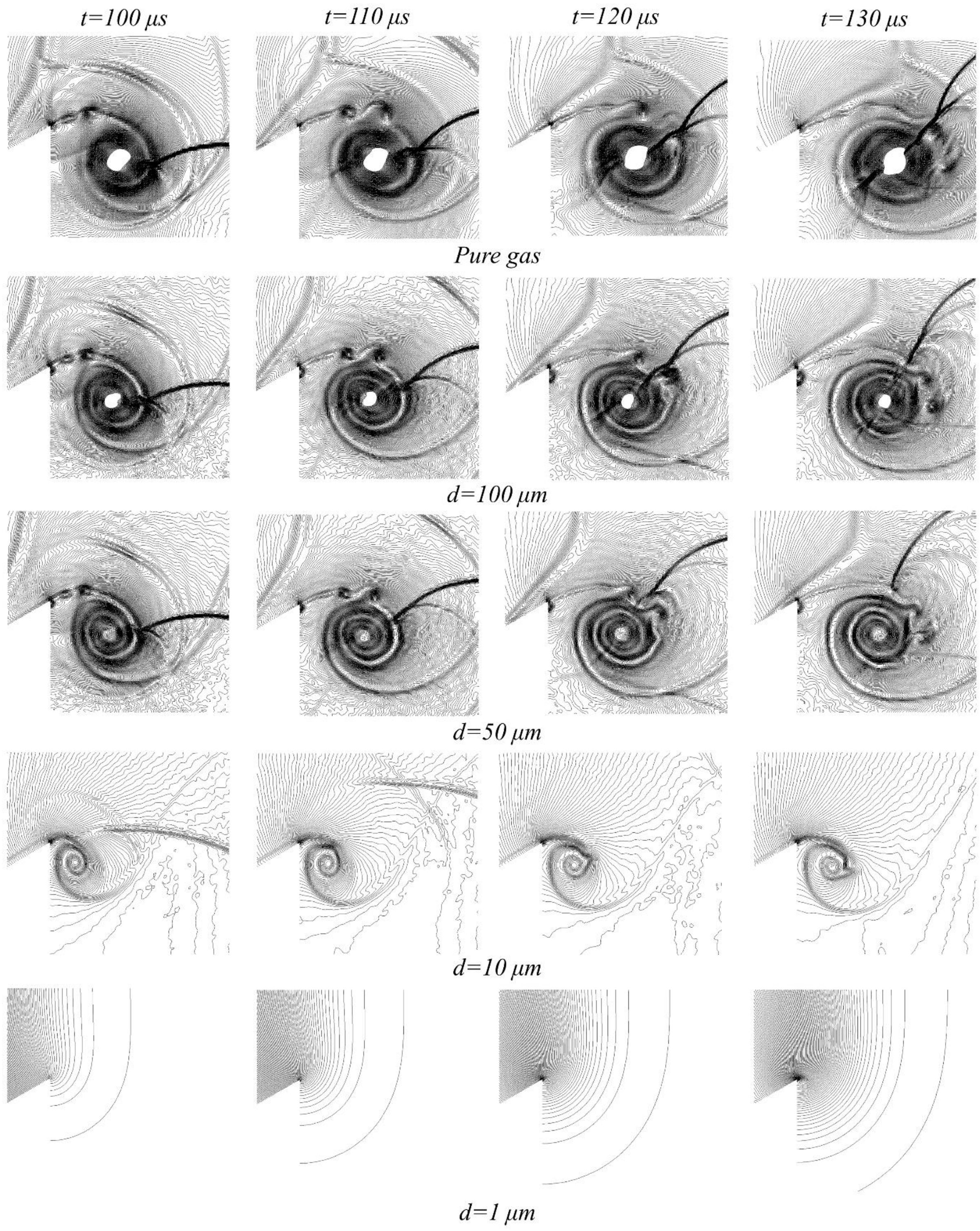

Fig. 13 Visualizing the effects of the addition different diameter size particles on the decay of vortexlets using density isopycnics β=10

Table 1 A survey of some of important studies on the shock-vortex interaction

Problems	Mathematical models	Numerical methods
Schardin's problem [11]	Euler	Finite element method-flux corrected transport scheme
Shock wave interaction with a single-vortex [12]	Navier-Stokes	Sixth-order finite difference
Shock wave interaction with a pair-vortex [4]	Navier-Stokes	Sixth-order finite difference
Shock wave interaction with a vortex ring [14]	Axisymmetric Euler	Third-order ENO
Schardin's problem [15, 16]	Euler	High-resolution TVD method and adaptive quadrilateral grids in a finite volume method
Shock-vortex interactions at high Mach numbers [19]	Euler	Marquina's scheme with the piecewise hyperbolic method (a piecewise hyperbolic ENO-type reconstruction technique)
Shock wave interaction with a strong vortex [13]	Navier-Stokes	Fifth-order finite difference WENO scheme
Microscale shock-vortex interaction [23]	Boltzmann	DSMC
Schardin's problem [18]	Navier-Stokes	Fifth-order MUSCL scheme
Shock wave interaction with a strong vortex [17]	Euler	Ninth-order WENO
Microscale shock-vortex interaction in monatomic/diatomic/polyatomic gas molecules [20, 21]	Navier-Stokes Nonlinear coupled constitutive relation (NCCR)	High-order discontinuous Galerkin

Table 2 Eulerian versus Lagrangian

Model	Strength	Shortcoming
Eulerian	· Easy incorporation of particle diffusion effects · Simple extendibility to multi-dimensional flows · A wide range of validity	· Numerical instabilities and diffusion · Large storage requirements for multiple particle sizes · Additional modeling for inter-particle interaction
Lagrangian	· Embodies the natural solution schemes for each phase · No numerical diffusion of the particulate phase · No excessive storage requirements for multiple particle sizes	· Need for empirical diffusion velocity or more expensive Monte Carlo methods · Complex to couple with Eulerian phase · Computationally expensive at high particulate loadings

Table 3 Parameters used in simulations

Parameter	Value
Carrier phase (air)	
Shock Mach number	1.34
Pressure (driver section)	195374.9 (Pa)
Temperature (driver section)	357.6396 (K)
Pressure (driven section)	101325 (Pa)
Dispersed phase (glass bead)	
Particle diameter (d)	1, 10, 50, 100 (μm)
Particulate loading (β)	1, 10
Particle density	2500 (kg/m^3)

* The values of the parameters at the driver section were considered as the reference values.

Table 4 Summary of important parameters in gas-particle flows

Term	Relation
Characteristic time	$t_{ref} = L_{ref} / \left\|\mathbf{u}_{ref}\right\|$
Particle momentum response time	$\tau_{\mathrm{V}} = \rho_s d^2 / (18\mu_g)$
Stokes number	$St = \tau_{\mathrm{V}} / t_{ref}$
Particulate loading	$\beta = \dot{m}_s / \dot{m}_g$
The physical interpretation of different Stokes regimes	
St >> 1	$\tau_{\mathrm{V}} >> t_{ref}$: Enough time for particles to equilibrate (one-way coupling).
St << 1	$\tau_{\mathrm{V}} << t_{ref}$: Particle velocity being little affected by the fluid velocity change, therefore remaining nearly equivalent velocities (two-way coupling).

- L_{ref} and $\mathbf{u}_{ref}$ represent the characteristic length and characteristic velocity, respectively.
- $\dot{m}_s$ and $\dot{m}_g$ denote particle mass flux and carrier phase mass flux, respectively.

Table 5 Summary of the main conclusions

Flow evolution steps		Developed features	
		Schardin’s problem	Dusty Schardin’s problem
1	Shock impingement on the prism	IS, MS_1, RS	Decelerated IS, MS_1, accelerated RS
2	Shock wave passage over prism’s tip	EF	Accelerated EF
3	Main vortex formation	V, MTP_1, SL_1	Displaced V*, MTP_1, SL_1*
4	Mach stems collision on the symmetry plane	RS, MS_2, SL_2	RS*, MS_2, SL_2
5	Shock-vortex interaction and scattering of reflected shock	AS, DS	Attenuated AS, attenuated DS
6	Vortexlet formation	DA, TS, VL	Attenuated DA*, TS*, VL*

AS = Accelerated Shock
DA = Diverging Acoustics
DS = Decelerated Shock
EF = Expansion Fan
IS = Incident Shock
MS = Mach Stem
MTP = Mach Triple Point
RS = Reflected Shock
SL = Slip Line
TS = Transmitted Shock
V = Vortex
VL = Vortexlet
* The feature is not apparent in high particulate loading or low diameter cases.